

Following the Crystallization of Amorphous Ice after Ultrafast Laser Heating

Marjorie Ladd-Parada,* Katrin Amann-Winkel, Kyung Hwan Kim, Alexander Späh, Fivos Perakis, Harshad Pathak, Cheolhee Yang, Daniel Mariedahl, Tobias Eklund, Thomas J. Lane, Seonju You, Sangmin Jeong, Matthew Weston, Jae Hyuk Lee, Intae Eom, Minseok Kim, Jaeku Park, Sae Hwan Chun, and Anders Nilsson



Cite This: *J. Phys. Chem. B* 2022, 126, 2299–2307



Read Online

ACCESS |



Metrics & More

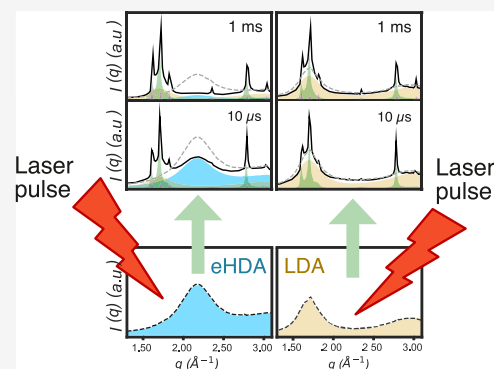


Article Recommendations



Supporting Information

ABSTRACT: Using time-resolved wide-angle X-ray scattering, we investigated the early stages (10 μ s–1 ms) of crystallization of supercooled water, obtained by the ultrafast heating of high- and low-density amorphous ice (HDA and LDA) up to a temperature $T = 205 \text{ K} \pm 10 \text{ K}$. We have determined that the crystallizing phase is stacking disordered ice (I_{sd}), with a maximum cubicity of $\chi = 0.6$, in agreement with predictions from molecular dynamics simulations at similar temperatures. However, we note that a growing small portion of hexagonal ice (I_{h}) was also observed, suggesting that within our timeframe, I_{sd} starts annealing into I_{h} . The onset of crystallization, in both amorphous ice, occurs at a similar temperature, but the observed final crystalline fraction in the LDA sample is considerably lower than that in the HDA sample. We attribute this discrepancy to the thickness difference between the two samples.



INTRODUCTION

Water crystallization is a phenomenon of utmost importance in a variety of areas, such as cloud formation,^{1–3} food preservation,^{4,5} and planetary sciences.⁶ Nevertheless, the early stages of water crystallization are not yet fully understood, especially in the temperature range between ca. 160 K⁷ and 232 K⁸ (often called “no man’s land”). The reason behind this is that water crystallizes spontaneously as either end of the regime is approached, thus making it challenging to induce and probe crystallization within no man’s land. However, different approaches have been used in an attempt to circumvent this problem and allow for experimental studies. By heating crystalline⁹ and amorphous ice,^{7,10–15} crystallization rates have been studied in the lower temperature region of “no man’s land” ($T = 134–160 \text{ K}$).^{6,13,14} Decreasing the sample size has been another approach as it hinders crystallization, allowing for the supercooling of water. Studies then use either nanoconfinement of water^{16–23} or cooling of micrometer^{24–28} or nanometer-sized^{29,30} droplets. Particularly, the use of microdroplets has allowed for the exploration of the nucleation rates down to 227 K,²⁴ whilst nanodroplets have helped explore temperatures down to 200 K. However, nanodroplets are affected by their high internal pressure and large surface to volume ratio, making it hard to connect their behavior to that of microdroplets.³¹

In a more recent study, transient heating of thin water films allowed for the estimation of nucleation rates at temperatures of $188 \text{ K} < T < 230 \text{ K}$.⁹ In this study, a maximum nucleation rate

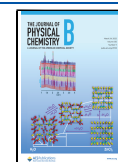
was observed at a temperature of $216 \text{ K} \pm 4 \text{ K}$, in agreement with nanodroplet experiments.³⁰ Importantly, it cannot be excluded that the observed crystallization might be surface-induced or even heterogeneous, as evidenced by recent studies of crystallization in nanodroplets between $T = 233 \text{ K}$ and $T = 235 \text{ K}$.³²

Whilst there has been a large focus on crystallization rates, it is also of interest to understand the nucleating crystal structure in “no man’s land”. The most stable crystalline phase of water at ambient pressure is that of hexagonal ice, I_{h} , (Figure 1A). However, a different polytype has also been reported, that is, stacking disordered ice, I_{sd} , (Figure 1B), which consists of randomly intercalated layers of cubic and hexagonal sequences. This crystalline form was originally referred to as cubic ice, I_{c} ,^{33,34} (Figure 1C). Nevertheless, it is evident from the X-ray scattering patterns, such as that shown in Figure 1B, that whilst it does display peaks related to a cubic phase (Figure 1C), it retains features of I_{h} , especially the peak denoted as P1 (Figure 1A).³⁵ One of the reasons why I_{sd} was often called I_{c} was because pure I_{c} had not been experimentally produced. Recently, two groups

Received: December 28, 2021

Revised: February 14, 2022

Published: March 11, 2022



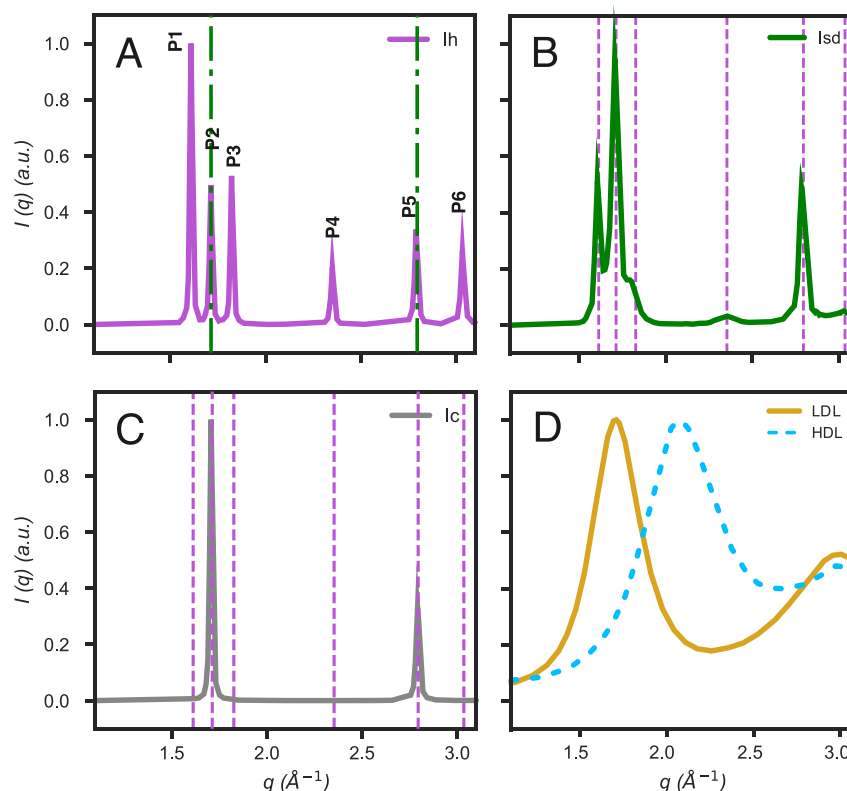


Figure 1. Typical diffraction patterns of (A) hexagonal ice (I_h), (B) an example of stacking disordered ice (I_{sd}) with 50% cubicity, (C) cubic ice (I_c), and (D) HDL (dashed blue line)¹⁵ and LDL (yellow continuous line).³⁸ Marked in dashed purple vertical lines are the peak positions of I_h , and in dashed-dotted green lines the peak positions of I_c . In Figure A, we have numbered the different peaks present in I_h , from P1 to P6, of which, P2 and P5 are the peak positions shared between I_h and I_c . Crystalline ice (A to C) scattering patterns were calculated using the FAULTS diffraction simulation software,³⁹ following the same procedure as with DIFFAX.³⁵

independently obtained pure I_c , showing the typical diffraction pattern of a cubic structure (Figure 1C),^{36,37} without any of the additional features of I_{sd} .

Experimentally, I_{sd} has been observed as the crystallizing form either at temperatures above 225 K or below 200 K.^{2,33,40–42} Whilst for temperatures between these two extremes it is only through molecular simulations^{43–47} that I_{sd} has been identified as the initial crystalline structure. Both through experiments and simulations,^{35,40,42} it has also been noted that the cubicity of I_{sd} decreases over time both at constant⁴² and increasing temperature,³⁵ leading to annealing into I_h , which is the thermodynamically stable phase.⁴²

Recently, two different studies^{15,48} have reported on the crystallization of ice directly from a low-density noncrystalline phase (LDN). By measuring in situ X-ray diffraction during rapid decompression of high-pressure ice,⁴⁸ a transition to an LDN between 140 and 165 K was observed. Eventually, the sample crystallized into I_{sd} . On the other hand, X-ray scattering studies, combined with a laser-induced T-jump,¹⁵ indicated a discontinuous transition between high and low-density liquid water (HDL and LDL, respectively) at $205 \text{ K} \pm 10 \text{ K}$, prior to the onset of crystallization, that is, within a time frame between 8 ns and $1 \mu\text{s}$. This transition was observed in the q -region between 1.1 and 2.5 \AA^{-1} , where the first-order peaks of both liquids are clearly observable: HDL (ca. 2.1 \AA^{-1}) and LDL (1.7 \AA^{-1}) (Figure 1B).

By looking at the nano- to microsecond scale, it was possible to open a window to observe the early stages of ice formation.¹⁵ Therefore, we have taken a deeper inspection into the later

delays ($10 \mu\text{s}$ onwards), from the same experiment, to explore the initial crystallizing forms in “no man’s land”. Within the observed timescale ($10 \mu\text{s}$ – 1 ms), water crystallizes in a stacking disordered manner with a high cubicity, in line with the results of Amaya et al.⁴⁰ This cubicity decreases over time, similar to previous experiments.^{21,23–25} Whilst I_{sd} is the main crystal structure, we observe that a small proportion of I_h was also present, suggesting that a fraction of the crystallites started transforming into this form.^{49,52}

METHODS AND MATERIALS

The experiments were conducted at the XSS-FXS beamline of PAL-XFEL, with 25 fs X-ray pulses with a mean energy of 9.7 keV and are described in detail by Kim et al.¹⁵ Here, we highlight some of the most important details.

Sample Preparation. In brief, amorphous ice samples were prepared inside a 0.1 mm-thick Cu-grid using a material testing machine (Zwick, Z100 TN).^{12,15,38,33} The grid was filled with ultrapure deionized water and precooled over liquid nitrogen to form crystalline ice. After cold-loading the grids into a piston cylinder setup and covering the grids with a thin In-foil, unannealed high-density amorphous ice was formed by pressurizing to 1.6 GPa at 100 K. The samples were then heated and annealed at 160 K and 1.1 GPa, resulting in very-high-density amorphous ice. For transformation into equilibrated high-density amorphous ice (eHDA) or low-density amorphous ice (LDA), the samples were decompressed at 139.5 K to 0.08 and 0.01 GPa, respectively, and subsequently quenched to 80 K. The resulting eHDA and LDA samples

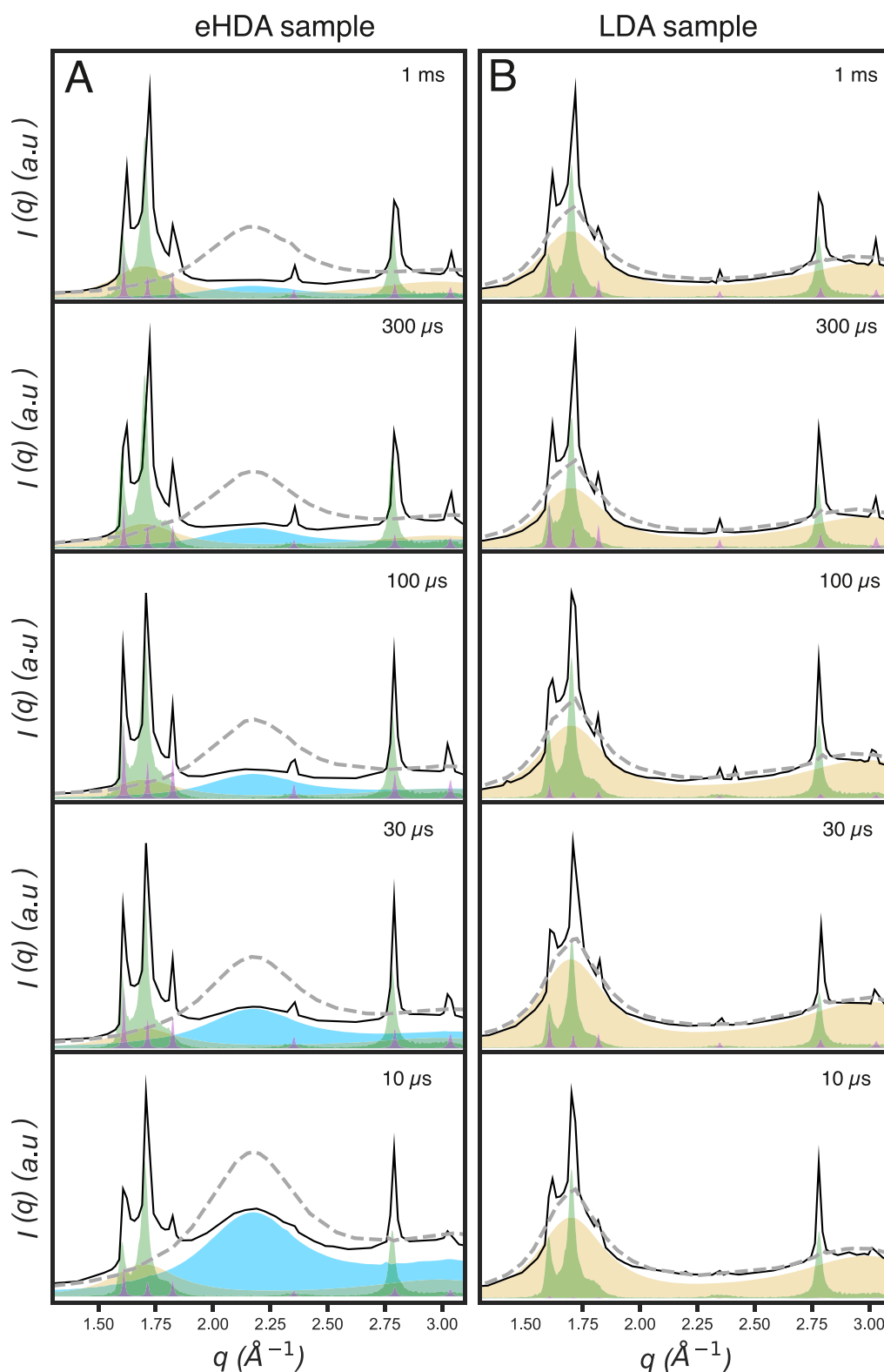


Figure 2. Time-resolved wide-angle X-ray scattering patterns showing the progression of crystallization from 10 μs to 1 ms. (A) eHDA at a base temperature of 115 K and (B) LDA at a base temperature of 140 K. Prepump scattering is shown as a gray dashed line and the postpump as a black continuous line. Contributions of the HDL are indicated in blue, LDL in yellow, I_{sd} in green, and I_{h} in purple.

were decompressed to ambient pressure, stored, and transported under liquid nitrogen temperatures to PAL-XFEL, South Korea.

Laser and X-ray Parameters. We utilized an infrared-pump X-ray probe scheme to obtain time-dependent single-shot X-ray scattering patterns. Samples were loaded on a sample

environment consisting of a liquid N_2 -flow cryostat capable of operating in vacuum between 80 K and room temperature.

The samples were then pumped by a 100 fs infrared (IR) pulse with a 2 μm wavelength, which excited a combination of O–H stretch and H–O–H bending modes that increased the

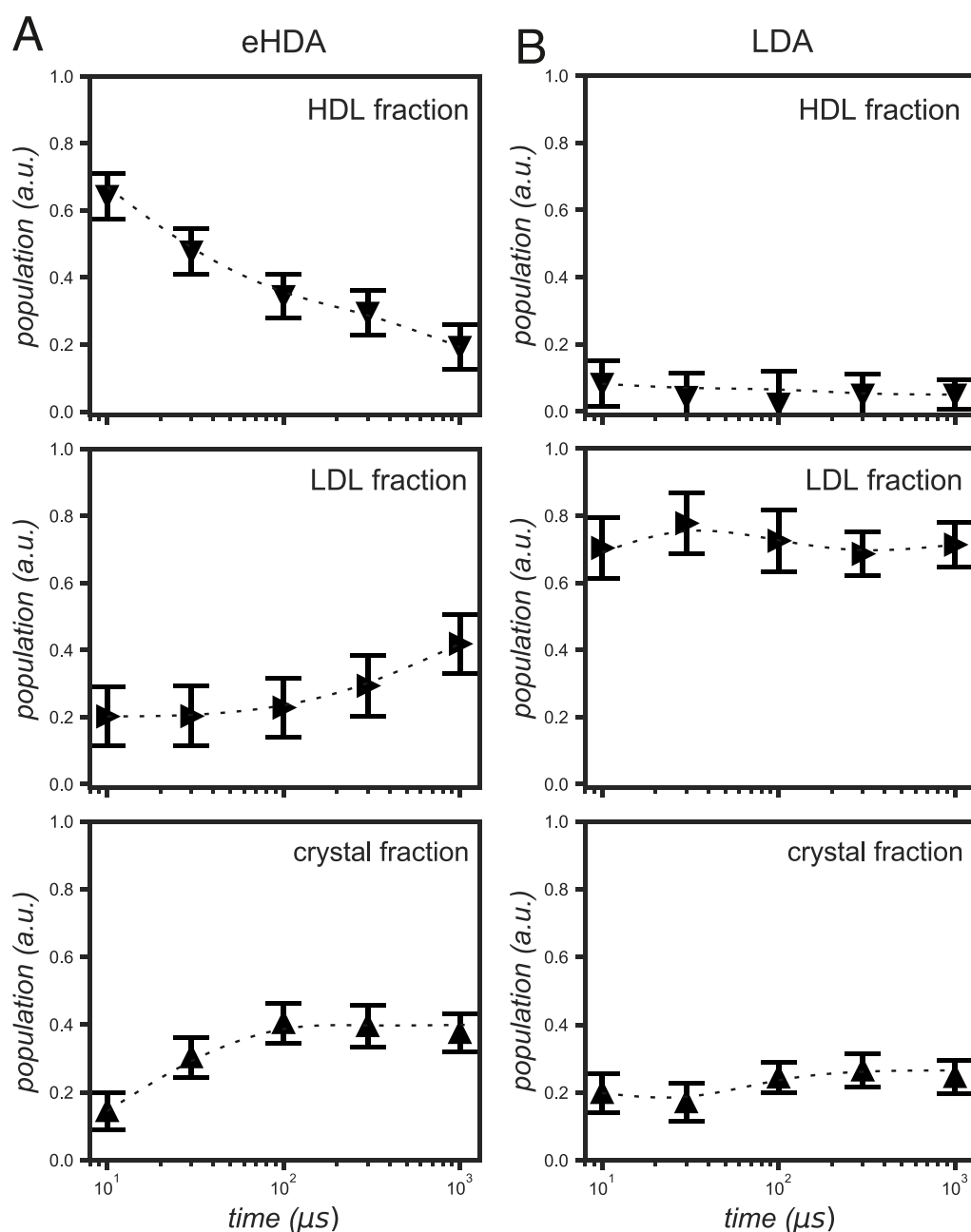


Figure 3. Time-dependent population changes from 10 μs to 1 ms. (A) Fractions of HDL, LDL, and crystalline ice taken from the fits of the (A) eHDA samples and of the (B) LDA samples. Downward triangles represent the HDL fractions, the right triangles the LDL fractions, and the upward triangles the crystalline ($I_h + I_{sd}$) fraction. Bars indicate the error of the fit. Dotted lines are added just as a guide to the eye.

temperature of the sample in ca. 20 ps,^{54,55} resulting in an ultrafast temperature-jump (T-jump) of about 90 K, in the case of HDA, and of 60 K for LDA,¹⁵ resulting in a final temperature of around 205 ± 10 K. Scattering images were taken at different delays to capture the whole T-jump. The images were taken in the wide-angle regime covering a q -range of 0.1–3.2 \AA^{-1} , allowing for the observation of the first diffraction peaks of the high- and low-density structures. Laser-off images were acquired and used as a reference, and for obtaining the time-resolved difference X-ray scattering patterns.

Data Analysis. The proportions of the different components (HDL, LDL, and crystalline ice) were estimated by fitting the time-dependent difference scattering curves, obtained by taking

the difference between the $I(q)$ curves measured before and after laser excitation (see the Supporting Information Figure S1).

We particularly focused on the relative amount of cubic vs hexagonal stacking. Different parameters were considered for this objective: the fraction of I_h (obtained from the fittings), the degree of cubicity, the ratio between P2 and P1, and the intensity of P4 at ca. 2.34 \AA^{-1} .

The degree of cubicity (χ) is defined as follows:^{35,41,42,56}

$$\chi = \frac{\varphi_{hc}}{\varphi_{hc} + \varphi_{ch}} \quad (1)$$

where φ_{hc} is the probability of a cubic layer to form over a hexagonal layer, and φ_{ch} is the probability of a hexagonal layer to form over a cubic layer. To obtain the P2:P1 ratio and the intensity of P4, the liquid (HDL and LDL) fractions were

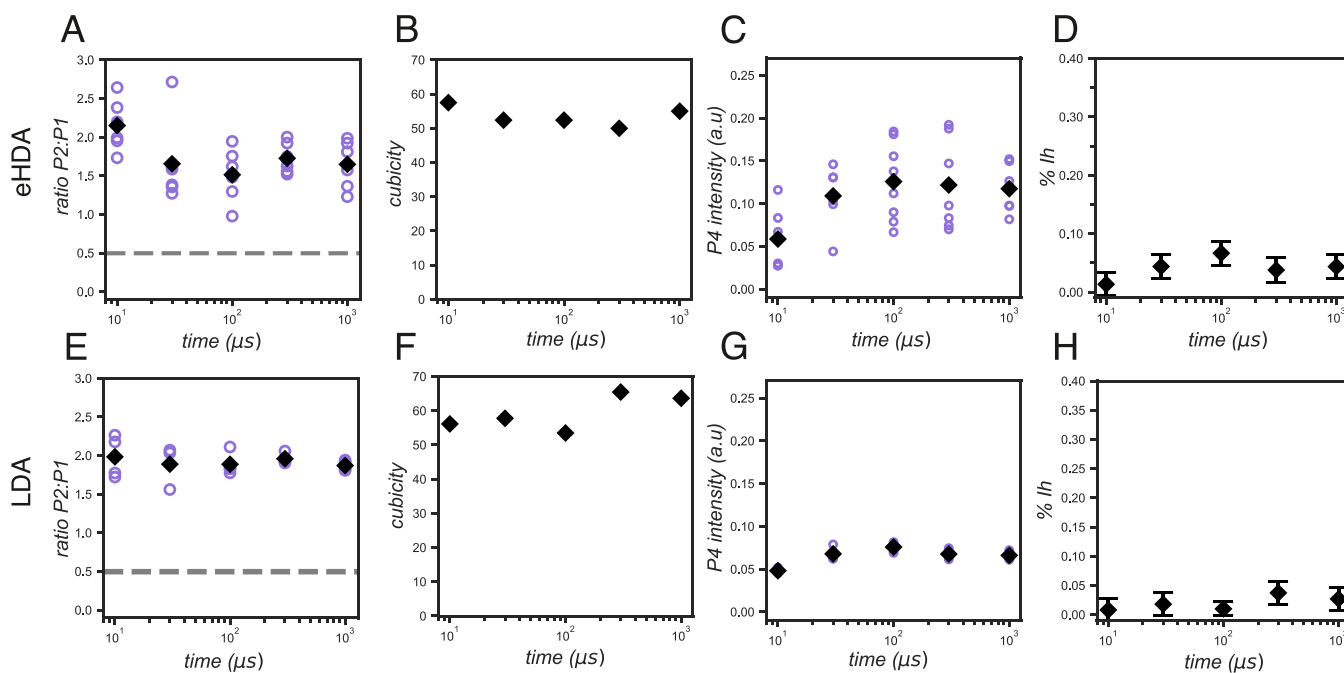


Figure 4. Ratio of P2:P1, cubicity (χ), intensity of P4, and % of I_h as a function of the delay time of (A to D) eHDA samples and (E to H) LDA samples. A dashed line has been added to the plots of the P2:P1 ratios (A and E) to indicate the ratio observed in a pure I_h scattering pattern. Values higher than this ratio (ca. 0.5) indicate a higher proportion of cubicity. Purple circles in the plots A, C, E, and G are the values for individual samples, and the black diamonds are the average of all the measurements. Bars in plots D and H indicate the error of the fit.

subtracted from the postpump shots (Figure S3). The P2:P1 ratio quantifies the degree of cubicity as P1 is unique to I_h , whereas P2 is shared between I_h and I_c . In pure I_h , the P2:P1 ratio is approximately 0.50,⁵⁰ and higher values indicate a larger amount of cubic stacking.^{51,52} In the case of P4, this peak is only present in pure I_h ; therefore, it can be used as a marker for hexagonal stacking.⁵⁰

Finally, from the obtained crystalline fraction, the nucleation and growth rates were roughly estimated for both samples, as detailed in the Supporting Information of Kim et al.¹⁵ using the following equation:

$$\text{population}(t) = 1 - e^{-\pi/3JG^3t^4} \quad (2)$$

where J is the nucleation rate, G is the growth rate, and t is time. It should be noted that the values of J and G vary with temperature.

We fitted the crystallization curves only up to 100 μs , as after this delay, cooling dominates.¹⁵ In the case of the eHDA sample, this leads to an apparent decrease in the crystalline fraction because of the increase in the LDL fraction. The fits were performed by leaving the growth rate as a free parameter, but fixing J to the value estimated by Kimmel et al.⁹ for 200 and 205 K, for the LDA and eHDA samples, respectively, as these are the estimated reached temperatures.¹⁵

RESULTS AND DISCUSSION

We performed measurements after different delay times between 8 ns and 1 ms. However, crystallization is only evident from 3 μs onward, and it is only from 10 μs that a good enough fit was possible. Therefore, we focus on these later delays where ice Bragg peaks are observable in both eHDA and LDA samples (Figure 2).

From the scattering patterns, it is already evident that in the eHDA sample (Figure 2A), the HDL fraction decreases over

time, as the broad peak centered at ca. 2.1 \AA^{-1} almost disappears by the 1 ms delay time. Crystallization, as expected, has the opposite behavior with increasing intensity of the crystalline Bragg peaks. In the LDA sample (Figure 2B), however, the decrease in the LDL fraction is not as dramatic as that of the HDL in the eHDA sample. However, crystallization increases as particularly evidenced by the intensity of P4 and P6 (ca. 2.3 and 3 \AA^{-1}).

We further fitted the difference scattering patterns with a linear combination of HDL, LDL, and crystalline ice (Figure S1). Importantly, for the crystalline ice fraction, we initially considered stacking disordered ice (I_{sd}) only, but it frequently underestimated the sharpness and height of P3 and P4, as shown in Figure S2A. Therefore, we decided to use a combination of simulated pure hexagonal ice (I_h) and I_{sd} , resulting in a better fit (Figure S2B). The improvement of the fit by the introduction of the diffraction pattern of I_h suggests that part of the I_{sd} has started to anneal into I_h and that we thus have a combination of two different crystalline ice.

In the eHDA sample (Figure 3A), we observe that the HDL fraction decreases continuously as it converts to LDL. However, we do not see a parallel increase in the LDL fraction. In fact, we see that the LDL fraction initially remains stable at a population fraction of ca. 0.20 and only increases from 100 μs onward. Nevertheless, the crystal fraction initially increases and then stabilizes at 100 μs . Consequently, we can infer that the apparent discrepancy between the LDL and HDL behavior is related to the progressing crystallization. Between 10 and 100 μs , the LDL constantly crystallizes; thus, the observable amount of LDL instantly decreases, even though we know that the HDL continuously transforms into LDL. From Kim et al.¹⁵ we know that considering the thermal diffusivity of our samples, we can estimate that prior to 100 μs , the temperature of the sample is stable. However, after 100 μs , the sample starts cooling again¹⁵ because of the rest of the sample being at 115 K, resulting in a

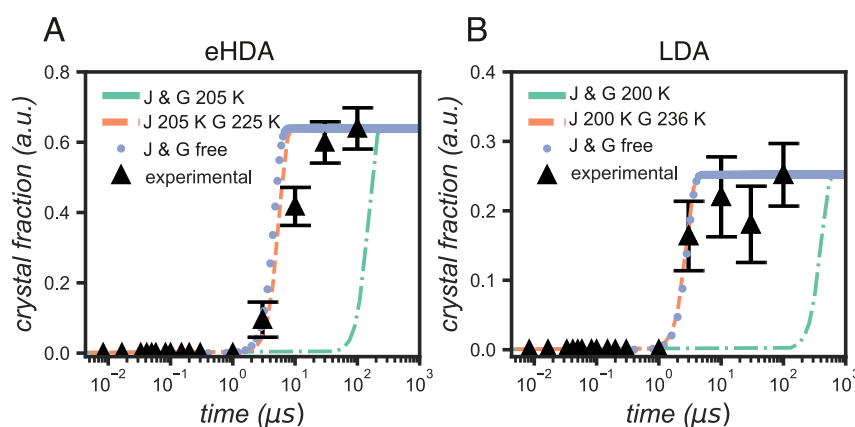


Figure 5. Crystallization curves of (A) the eHDA sample and (B) the LDA sample. Black triangles are the experimental data. Dotted blue line is the corresponding fit where the nucleation rate, J , was fixed to the values from Kimmel et al.⁹ at 205 and 200 K for the eHDA and LDA samples, respectively. Dashed orange line shows the theoretical crystallization curve using the same J ⁹ as before, and the growth rate, G , from Xu et al.⁶³ closest to the estimated G from the blue fit (i.e., the G at 225 and 235 K for the eHDA and LDA samples, respectively). Dashed-dotted green line is the theoretical crystallization curve using J ⁹ and G ⁶³ at the estimated temperature for each sample.

higher viscosity that hampers crystallization, thus allowing us to see the growth in the LDL fraction once more.

In the LDA sample (Figure 3B), the crystalline fraction initially increases between 30 and 100 μs but remains stable after this delay, which is also attributable to the estimated cooling. Whilst the overall trend is similar to that of the eHDA sample, we note that the final crystal fraction is considerably smaller and that consequently the liquid fraction is higher. The reduced crystalline fraction is most likely caused by our LDA samples being thicker (>55 μm) than those of eHDA (35–55 μm). This larger thickness causes the front part of the sample to absorb more heating light than the back, thus creating a larger temperature difference between the two sides of the sample, which can lead to a faster cooling from 100 μs onward. Moreover, we cannot exclude that the transition from HDL to LDL has an exothermic character, causing a further temperature increase, thus accelerating crystallization in the eHDA sample. Finally, we also observe a minor fraction of HDL (Figure 3B) but with error bars going down to negative values at most delay times. Thus, we do not consider it to be of particular significance.

We also note that, even at 1 ms, both samples retain fractions of both LDL and HDL, in agreement with previous studies where a coexistence between crystalline ice and supercooled water has been reported even after several seconds.^{6,57–60} These results differ from those of Kim et al.¹⁵ in that study, and it was assumed that the sample was completely crystalline after 1 ms. However, the focus of that study was on the earlier delays (before 10 μs), where the HDL to LDL transition occurs, and the proportion of crystalline ice is either nonexistent or insignificant. Thus, the assumption of a fully crystalline sample at 1 ms is consistent with the conclusions there reached.

As mentioned before, the main crystal form obtained was that of I_{sd} , and from the fitted scattering patterns, we were able to estimate the relative amount of cubic and hexagonal stacking present in the sample. We used different approaches for this purpose. We evaluated the ratio between P2 and P1, the degree of cubicity, the intensity of P4, and the fraction of I_{h} (Figure 4).

In the eHDA sample, the P2:P1 ratio (Figure 4A) initially decreases and stabilizes after 100 μs . As expected, the intensity of P4 consequently increases and stabilizes after the same time delay (Figure 4B), suggesting that the relative amount of hexagonal stacking increases at the expense of the cubic stacking.

Similar trends are observed in the cubicity and fraction of I_{h} (Figure 4C, D).

In the LDA sample, the P2:P1 ratio remains at a similar level to that of eHDA at 10 μs (Figure 4E), whilst the intensity of P4 increases slightly between 10 and 100 μs , after which it remains stable (Figure 4F), suggesting an initial minor increase in hexagonal packing. Notably, the degree of cubicity increases slightly at higher delay times, alongside the fraction of I_{h} (Figure 4F, H), which is surprising as we would expect them to be inversely related, not to mention that this trend was not observed in the P2:P1 ratio, nor in the P4 intensity. The behavior of the cubicity and I_{h} might then be an effect of the fitting itself. In the LDA scattering patterns, P5 has a strong intensity (Figure S3), sometimes almost equal to P2, suggesting a preferred orientation of the crystal, which is not considered in our I_{sd} simulations. Therefore, our fitting could be overestimating the amount of I_{h} in an attempt to reach the higher intensity of P5 in the experimental data. As a consequence, other I_{h} peaks would have higher intensities than those experimentally obtained, and a higher cubicity I_{sd} would then be necessary to compensate. Nevertheless, given that the P2:P1 ratio and P4 intensities are in agreement, we consider that our fits are still a good indicator of the overall trend of increase in hexagonal stacking up to 100 μs .

Lastly, the cubicities here estimated are in agreement with previous molecular simulations at similar temperatures,^{43,45,61} reporting values between 0.60 and 0.70. Experimentally, cubicities have mostly been reported to reach a maximum of 0.5,^{42,62} except for the work by Malkin et al.,³⁵ who reported a cubicity of 0.78 when recrystallizing ice II into ice I. Amaya et al.⁴⁰ also estimated a cubicity close to 0.80 at 225 K, which they attribute to both the low temperature and the faster crystallization observed in nanodroplets.³⁰

Finally, we performed fits based on the nucleation data from Kimmel et al.⁹ and the growth rate data from Xu et al.⁶³ to evaluate them in the current system. By fixing the nucleation rate (J) to the values from Kimmel et al.⁹ at the estimated temperatures, for each sample (205 and 200 K for eHDA and LDA, respectively), we obtained, for eHDA, a growth rate close to that estimated by Xu et al. at 225 K⁶³ (see Table S1), that is, 20 K above the estimated T-jump. In comparison, the fit for the LDA sample resulted in a growth rate close to that at 235 K, that

is, 35 K above the estimated T-jump. The temperature difference between nucleation rate J and growth rate G can be assumed to originate from the heat release during the nucleation process, leading to crystal growth occurring at a different temperature. This is further reinforced by the estimated temperature increase because of crystallization between 17.5 and 39.5 K (see the Supporting Information), assuming that there is no heat release to the environment because of the timescales studied here.^{64,65} The estimated temperature increase is in the same order of magnitude as the increase in temperature assumed by using the growth rates at 20 and 36 K higher than the nucleation rates.

After the first crystallization point at 3 μ s, the experimental data follow a slower crystallization rate than the fits (Figure 5). In the case of the eHDA sample, this can be explained by crystallization not happening in the bulk, but only in the new LDL domains. As the crystalline material grows within these domains, crystallites can eventually impinge on each other, slowing the growth rate. In the case of the LDA sample, we could expect bulklike crystallization as the whole sample is considered to have converted into LDL. Nevertheless, we have estimated that LDA samples have a larger thickness (>55 μ m) than the eHDA (35–55 μ m), leading to further cooling from the back side of the sample, which has not been heated to the same degree. This cooling then reduces the growth rate as the viscosity of the liquid increases, hindering crystallization. Further evidence of the hindering of crystallization can be found in the final crystalline fraction. The LDA samples only reach a fraction of ca. 0.25, in comparison to the eHDA samples that reached almost 0.6.

CONCLUSIONS

Within the timescales evaluated in this study, we observe that the crystallization of LDL coming from heating either HDA or LDA occurs in the microsecond scale in a stacking disorder form (I_{sd}) with a large cubicity (0.5–0.65), which decreases over time. Nevertheless, even in these short timescales, some of the ice anneals into I_h , the thermodynamically preferred crystalline state,⁴² leading to a mix of I_{sd} and I_h . The crystallization of the LDA sample stagnated from 30 μ s onward, thus reaching a lower final crystalline fraction than the eHDA sample. We ascribe this to the larger thickness of the LDA samples. Finally, while the first crystallization points are correctly fitted by using literature nucleation values at the estimated sample temperatures, the estimated growth rate is equivalent to values at higher temperatures, which could be attributed to the heat release during nucleation.

ASSOCIATED CONTENT

Supporting Information

The Supporting Information is available free of charge at <https://pubs.acs.org/doi/10.1021/acs.jpcb.1c10906>.

Difference scattering curves and their fits, calculation of the P4 intensities, P2:P1 ratios, nucleation and growth rates used in Figure 5, and estimation of the temperature increase due to crystallization (PDF)

AUTHOR INFORMATION

Corresponding Author

Marjorie Ladd-Parada – Department of Physics, AlbaNova University Center, Stockholm University, Stockholm SE-

10691, Sweden; orcid.org/0000-0003-1355-649X;
Email: marjorie.ladd-parada@fysik.su.se

Authors

- Katrin Amann-Winkel** – Department of Physics, AlbaNova University Center, Stockholm University, Stockholm SE-10691, Sweden; orcid.org/0000-0002-7319-7807
- Kyung Hwan Kim** – Department of Chemistry, POSTECH, Pohang 37673, Republic of Korea
- Alexander Späh** – Department of Physics, AlbaNova University Center, Stockholm University, Stockholm SE-10691, Sweden; SLAC National Accelerator Laboratory, Menlo Park, California 94025, United States
- Fivos Perakis** – Department of Physics, AlbaNova University Center, Stockholm University, Stockholm SE-10691, Sweden; orcid.org/0000-0001-9863-9811
- Harshad Pathak** – Department of Physics, AlbaNova University Center, Stockholm University, Stockholm SE-10691, Sweden
- Cheolhee Yang** – Department of Chemistry, POSTECH, Pohang 37673, Republic of Korea
- Daniel Mariedahl** – Department of Physics, AlbaNova University Center, Stockholm University, Stockholm SE-10691, Sweden
- Tobias Eklund** – Department of Physics, AlbaNova University Center, Stockholm University, Stockholm SE-10691, Sweden
- Thomas J. Lane** – SLAC National Accelerator Laboratory, Menlo Park, California 94025, United States
- Seonju You** – Department of Chemistry, POSTECH, Pohang 37673, Republic of Korea
- Sangmin Jeong** – Department of Chemistry, POSTECH, Pohang 37673, Republic of Korea
- Matthew Weston** – Department of Physics, AlbaNova University Center, Stockholm University, Stockholm SE-10691, Sweden
- Jaе Hyuk Lee** – Pohang Accelerator Laboratory, Pohang, Gyeongbuk 37673, Republic of Korea
- Intae Eom** – Pohang Accelerator Laboratory, Pohang, Gyeongbuk 37673, Republic of Korea
- Minseok Kim** – Pohang Accelerator Laboratory, Pohang, Gyeongbuk 37673, Republic of Korea
- Jaеku Park** – Pohang Accelerator Laboratory, Pohang, Gyeongbuk 37673, Republic of Korea
- Sae Hwan Chun** – Pohang Accelerator Laboratory, Pohang, Gyeongbuk 37673, Republic of Korea
- Anders Nilsson** – Department of Physics, AlbaNova University Center, Stockholm University, Stockholm SE-10691, Sweden; orcid.org/0000-0003-1968-8696

Complete contact information is available at:
<https://pubs.acs.org/doi/10.1021/acs.jpcb.1c10906>

Author Contributions

The manuscript was written through contributions of all authors. All authors have given approval to the final version of the manuscript.

Notes

The authors declare no competing financial interest.

ACKNOWLEDGMENTS

This work has been supported by a European Research Council Advanced Grant under project 667205 and the Swedish National Research Council. K.A.-W. acknowledges funding by the Ragnar Söderbergs Stiftelse. T.J.L. was supported by the U.S.

Department of Energy contract DE-AC02-76SF00515. This work is also supported by the National Research Foundation of Korea (NRF) grant funded by the Korea government (MSIT) (2019R1C1C1006643). The experiments were performed at the beamline XSS of PAL-XFEL (proposal 2019-1st-XSS-008) funded by the Korea government (MSIT).

REFERENCES

- (1) Murray, B. J.; Jensen, E. J. Homogeneous Nucleation of Amorphous Solid Water Particles in the Upper Mesosphere. *J. Atmos. Sol. Terr. Phys.* **2010**, *72*, 51–61.
- (2) Murray, B. J.; Malkin, T. L.; Salzmann, C. G. The Crystal Structure of Ice under Mesospheric Conditions. *J. Atmos. Sol. Terr. Phys.* **2015**, *127*, 78–82.
- (3) Hudait, A.; Molinero, V. What Determines the Ice Polymorph in Clouds? *J. Am. Chem. Soc.* **2016**, *138*, 8958–8967.
- (4) You, Y.; Kang, T.; Jun, S. Control of Ice Nucleation for Subzero Food Preservation. *Food Eng. Rev.* **2021**, *13*, 15–35.
- (5) Dalvi-Isfahan, M.; Hamdami, N.; Xanthakis, E.; Le-Bail, A. Review on the Control of Ice Nucleation by Ultrasound Waves, Electric and Magnetic Fields. *J. Food Eng.* **2017**, *195*, 222–234.
- (6) Jenniskens, P.; Blake, D. F. Crystallization of Amorphous Water Ice in the Solar System. *Astrophys. J.* **1996**, *473*, 1104–1113.
- (7) Smith, R. S.; Kay, B. D. The Existence of Supercooled Liquid Water at 150?K. *Nature* **1999**, *398*, 788–791.
- (8) Mason, B. J. The Supercooling and Nucleation of Water. *Adv. Phys.* **1958**, *7*, 221–234.
- (9) Kimmel, G. A.; Xu, Y.; Brumberg, A.; Petrik, N. G.; Smith, R. S.; Kay, B. D. Homogeneous Ice Nucleation Rates and Crystallization Kinetics in Transiently-Heated, Supercooled Water Films from 188 K to 230 K. *J. Chem. Phys.* **2019**, *150*, 204509.
- (10) Johari, G. P.; Hallbrucker, A.; Mayer, E. The Glass–Liquid Transition of Hyperquenched Water. *Nature* **1987**, *330*, 552–553.
- (11) Andersson, O. Glass–Liquid Transition of Water at High Pressure. *Proc. Natl. Acad. Sci. U. S. A.* **2011**, *108*, 11013–11016.
- (12) Kim, K. H.; Späh, A.; Pathak, H.; Perakis, F.; Mariedahl, D.; Amann-Winkel, K.; Sellberg, J. A.; Lee, J. H.; Kim, S.; Park, J.; Nam, K. H.; Katayama, T.; Nilsson, A. Maxima in the Thermodynamic Response and Correlation Functions of Deeply Supercooled Water. *Science* **2017**, *358*, 1589–1593.
- (13) Safarik, D. J.; Mullins, C. B. The Nucleation Rate of Crystalline Ice in Amorphous Solid Water. *J. Chem. Phys.* **2004**, *121*, 6003.
- (14) Kondo, T.; Kato, H. S.; Bonn, M.; Kawai, M. Morphological Change during Crystallization of Thin Amorphous Solid Water Films on Ru(0001). *J. Chem. Phys.* **2007**, *126*, 181103.
- (15) Kim, K. H.; Amann-Winkel, K.; Giovambattista, N.; Späh, A.; Perakis, F.; Pathak, H.; Parada, M. L.; Yang, C.; Mariedahl, D.; Eklund, T.; Lane, T. J.; You, S.; Jeong, S.; Weston, M.; Lee, J. H.; Eom, I.; Kim, M.; Park, J.; Chun, S. H.; Poole, P. H.; Nilsson, A. Experimental Observation of the Liquid-Liquid Transition in Bulk Supercooled Water under Pressure. *Science* **2020**, *370*, 978–982.
- (16) Mallamace, F.; Corsaro, C.; Baglioni, P.; Fratini, E.; Chen, S.-H. The Dynamical Crossover Phenomenon in Bulk Water, Confined Water and Protein Hydration Water. *J. Phys. Condens. Matter* **2012**, *24*, No. 064103.
- (17) Mishima, O.; Stanley, H. E. Decompression-Induced Melting of Ice IV and the Liquid–Liquid Transition in Water. *Nature* **1998**, *392*, 164–168.
- (18) Mishima, O. Liquid-Liquid Critical Point in Heavy Water. *Phys. Rev. Lett.* **2000**, *85*, 334–336.
- (19) Chen, S.-H.; Mallamace, F.; Mou, C.-Y.; Broccio, M.; Corsaro, C.; Faraone, A.; Liu, L. The Violation of the Stokes–Einstein Relation in Supercooled Water. *Proc. Natl. Acad. Sci. U. S. A.* **2006**, *103*, 12974–12978.
- (20) Cupane, A.; Fomina, M.; Piazza, I.; Peters, J.; Schirò, G. Experimental Evidence for a Liquid-Liquid Crossover in Deeply Cooled Confined Water. *Phys. Rev. Lett.* **2014**, *113*, No. 215701.
- (21) Kim, C. U.; Barstow, B.; Tate, M. W.; Gruner, S. M. Evidence for Liquid Water during the High-Density to Low-Density Amorphous Ice Transition. *Proc. Natl. Acad. Sci. U. S. A.* **2009**, *106*, 4596–4600.
- (22) Chen, S. H.; Liu, L.; Fratini, E.; Baglioni, P.; Faraone, A.; Mamontov, E. Observation of Fragile-to-Strong Dynamic Crossover in Protein Hydration Water. *Proc. Natl. Acad. Sci. U. S. A.* **2006**, *103*, 9012–9016.
- (23) Kumar, P. Breakdown of the Stokes-Einstein Relation in Supercooled Water. *Proc. Natl. Acad. Sci. U. S. A.* **2006**, *103*, 12955–12956.
- (24) Laksmono, H.; McQueen, T. A.; Sellberg, J. A.; Loh, N. D.; Huang, C.; Schlesinger, D.; Sierra, R. G.; Hampton, C. Y.; Nordlund, D.; Beye, M.; et al. Anomalous Behavior of the Homogeneous Ice Nucleation Rate in “No-Man’s Land.”. *J. Phys. Chem. Lett.* **2015**, *6*, 2826–2832.
- (25) Riechers, B.; Wittbracht, F.; Hütten, A.; Koop, T. The Homogeneous Ice Nucleation Rate of Water Droplets Produced in a Microfluidic Device and the Role of Temperature Uncertainty. *Phys. Chem. Chem. Phys.* **2013**, *15*, 5873.
- (26) Kabath, P.; Stöckel, P.; Lindinger, A.; Baumgärtel, H. The Nucleation of Ice in Supercooled D₂O and H₂O. *J. Mol. Liq.* **2006**, *125*, 204–211.
- (27) Earle, M. E.; Kuhn, T.; Khalizov, A. F.; Sloan, J. J. Volume Nucleation Rates for Homogeneous Freezing in Supercooled Water Microdroplets: Results from a Combined Experimental and Modelling Approach. *Atmos. Chem. Phys.* **2010**, *10*, 7945–7961.
- (28) Wood, S. E.; Baker, M. B.; Swanson, B. D. Instrument for Studies of Homogeneous and Heterogeneous Ice Nucleation in Free-Falling Supercooled Water Droplets. *Rev. Sci. Instrum.* **2002**, *73*, 3988.
- (29) Manka, A.; Pathak, H.; Tanimura, S.; Wölk, J.; Strey, R.; Wyslouzil, B. E. Freezing Water in No-Man’s Land. *Phys. Chem. Chem. Phys.* **2012**, *14*, 4505.
- (30) Amaya, A. J.; Wyslouzil, B. E. Ice Nucleation Rates near ~225 K. *J. Chem. Phys.* **2018**, *148*, No. 084501.
- (31) Espinosa, J. R.; Vega, C.; Sanz, E. Homogeneous Ice Nucleation Rate in Water Droplets. *J. Phys. Chem. C* **2018**, *122*, 22892–22896.
- (32) Xue, H.; Fu, Y.; Lu, Y.; Hao, D.; Li, K.; Bai, G.; Ou-Yang, Z.-C.; Wang, J.; Zhou, X. Spontaneous Freezing of Water between 233 and 235 K Is Not Due to Homogeneous Nucleation. *J. Am. Chem. Soc.* **2021**, *143*, 13548–13556.
- (33) Sugisaki, M.; Suga, H.; Seki, S. Calorimetric Study of the Glassy State. IV. Heat Capacities of Glassy Water and Cubic Ice. *Bull. Chem. Soc. Jpn.* **1968**, *41*, 2591–2599.
- (34) Hallbrucker, A.; Mayer, E. Calorimetric Study of the Vitrified Liquid Water to Cubic Ice Phase Transition. *J. Phys. Chem.* **1987**, *91*, 503–505.
- (35) Malkin, T. L.; Murray, B. J.; Salzmann, C. G.; Molinero, V.; Pickering, S. J.; Whale, T. F. Stacking Disorder in Ice I. *Phys. Chem. Chem. Phys.* **2015**, *17*, 60–76.
- (36) Komatsu, K.; Machida, S.; Noritake, F.; Hattori, T.; Sano-Furukawa, A.; Yamane, R.; Yamashita, K.; Kagi, H. Ice Ic without Stacking Disorder by Evacuating Hydrogen from Hydrogen Hydrate. *Nat. Commun.* **2020**, *11*, 464.
- (37) del Rosso, L.; Celli, M.; Grazzi, F.; Catti, M.; Hansen, T. C.; Fortes, A. D.; Ulivi, L. Cubic Ice Ic without Stacking Defects Obtained from Ice XVII. *Nat. Mater.* **2020**, *19*, 663–668.
- (38) Mariedahl, D.; Perakis, F.; Späh, A.; Pathak, H.; Kim, K. H.; Camisasca, G.; Schlesinger, D.; Benmore, C.; Pettersson, L. G. M.; Nilsson, A.; et al. X-Ray Scattering and O–O Pair-Distribution Functions of Amorphous Ices. *J. Phys. Chem. B* **2018**, *122*, 7616–7624.
- (39) Casas-Cabanas, M.; Reynaud, M.; Rikarte, J.; Horbach, P.; Rodríguez-Carvajal, J. FAULTS: A Program for Refinement of Structures with Extended Defects. *J. Appl. Crystallogr.* **2016**, *49*, 2259–2269.
- (40) Amaya, A. J.; Pathak, H.; Modak, V. P.; Laksmono, H.; Loh, N. D.; Sellberg, J. A.; Sierra, R. G.; McQueen, T. A.; Hayes, M. J.; Williams, G. J.; et al. How Cubic Can Ice Be? *J. Phys. Chem. Lett.* **2017**, *8*, 3216–3222.

- (41) Malkin, T. L.; Murray, B. J.; Brukhno, A. V.; Anwar, J.; Salzmann, C. G. Structure of Ice Crystallized from Supercooled Water. *Proc. Natl. Acad. Sci. U. S. A.* **2012**, *109*, 1041–1045.
- (42) Kuhs, W. F.; Sippel, C.; Falenty, A.; Hansen, T. C. Extent and Relevance of Stacking Disorder in “Ice Ic”. *Proc. Natl. Acad. Sci. U. S. A.* **2012**, *109*, 21259–21264.
- (43) Moore, E. B.; Molinero, V. Is It Cubic? Ice Crystallization from Deeply Supercooled Water. *Phys. Chem. Chem. Phys.* **2011**, *13*, 20008.
- (44) Lupi, L.; Hudait, A.; Peters, B.; Grünwald, M.; Gotchy Mullen, R.; Nguyen, A. H.; Molinero, V. Role of Stacking Disorder in Ice Nucleation. *Nature* **2017**, *551*, 218–222.
- (45) Johnston, J. C.; Molinero, V. Crystallization, Melting, and Structure of Water Nanoparticles at Atmospherically Relevant Temperatures. *J. Am. Chem. Soc.* **2012**, *134*, 6650–6659.
- (46) Moore, E. B.; Molinero, V. Ice Crystallization in Water’s “No-Man’s Land”. *J. Chem. Phys.* **2010**, *132*, 244504.
- (47) Bullock, G.; Molinero, V. Low-Density Liquid Water Is the Mother of Ice: On the Relation between Mesostructure, Thermodynamics and Ice Crystallization in Solutions. *Faraday Discuss.* **2014**, *167*, 371–388.
- (48) Lin, C.; Smith, J. S.; Sinogeikin, S. V.; Shen, G. Experimental Evidence of Low-Density Liquid Water upon Rapid Decompression. *Proc. Natl. Acad. Sci. U. S. A.* **2018**, *115*, 2010–2015.
- (49) Johari, G. P. On the Coexistence of Cubic and Hexagonal Ice between 160 and 240 K. *Philos. Mag. B* **1998**, *78*, 375–383.
- (50) Murray, B. J.; Bertram, A. K. Formation and Stability of Cubic Ice in Water Droplets. *Phys. Chem. Chem. Phys.* **2006**, *8*, 186–192.
- (51) Kuhs, W. F.; Bliss, D. V.; Finney, J. L. High-Resolution Neutron Powder Diffraction Study of Ice Ic. *J. Phys. Colloq.* **1987**, *48*, C1-631–C1-636.
- (52) Hansen, T. C.; Koza, M. M.; Lindner, P.; Kuhs, W. F. Formation and Annealing of Cubic Ice: II. Kinetic Study. *J. Phys. Condens. Matter* **2008**, *20*, No. 285105.
- (53) Winkel, K.; Mayer, E.; Loerting, T. Equilibrated High-Density Amorphous Ice and Its First-Order Transition to the Low-Density Form. *J. Phys. Chem. B* **2011**, *115*, 14141–14148.
- (54) Ramasesha, K.; De Marco, L.; Mandal, A.; Tokmakoff, A. Water Vibrations Have Strongly Mixed Intra- and Intermolecular Character. *Nat. Chem.* **2013**, *5*, 935–940.
- (55) Iglev, H.; Schmeisser, M.; Simeonidis, K.; Thaller, A.; Laubereau, A. Ultrafast Superheating and Melting of Bulk Ice. *Nature* **2006**, *439*, 183–186.
- (56) Hansen, T. C.; Koza, M. M.; Kuhs, W. F. Formation and Annealing of Cubic Ice: I. Modelling of Stacking Faults. *J. Phys. Condens. Matter* **2008**, *20*, No. 285104.
- (57) Dowell, L. G.; Rinfret, A. P. Low-Temperature Forms of Ice as Studied by X-Ray Diffraction. *Nature* **1960**, *188*, 1144–1148.
- (58) Jenniskens, P.; Banham, S. F.; Blake, D. F.; McCoustra, M. R. S. Liquid Water in the Domain of Cubic Crystalline Ice Ic. *J. Chem. Phys.* **1997**, *107*, 1232–1241.
- (59) Dohnálek, Z.; Kimmel, G. A.; Ciolli, R. L.; Stevenson, K. P.; Smith, R. S.; Kay, B. D. The Effect of the Underlying Substrate on the Crystallization Kinetics of Dense Amorphous Solid Water Films. *J. Chem. Phys.* **2000**, *112*, 5932–5941.
- (60) Kohl, I.; Mayer, E.; Hallbrucker, A. The Glassy Water-Cubic Ice System : A Comparative Study by X-Ray Diffraction and Differential Scanning Calorimetry. *Phys. Chem. Chem. Phys.* **2000**, *2*, 1579–1586.
- (61) Hudait, A.; Qiu, S.; Lupi, L.; Molinero, V. Free Energy Contributions and Structural Characterization of Stacking Disordered Ices. *Phys. Chem. Chem. Phys.* **2016**, *18*, 9544–9553.
- (62) Broadley, S. L.; Murray, B. J.; Herbert, R. J.; Atkinson, J. D.; Dobbie, S.; Malkin, T. L.; Condliffe, E.; Neve, L. Immersion Mode Heterogeneous Ice Nucleation by an Illite Rich Powder Representative of Atmospheric Mineral Dust. *Atmos. Chem. Phys.* **2012**, *12*, 287–307.
- (63) Xu, Y.; Petrik, N. G.; Smith, R. S.; Kay, B. D.; Kimmel, G. A. Growth Rate of Crystalline Ice and the Diffusivity of Supercooled Water from 126 to 262 K. *Proc. Natl. Acad. Sci. U. S. A.* **2016**, *113*, 14921–14925.
- (64) Buttersack, T.; Bauerecker, S. Critical Radius of Supercooled Water Droplets: On the Transition toward Dendritic Freezing. *J. Phys. Chem. B* **2016**, *120*, 504–512.
- (65) Bauerecker, S.; Ulbig, P.; Buch, V.; Vrbka, L.; Jungwirth, P. Monitoring Ice Nucleation in Pure and Salty Water via High-Speed Imaging and Computer Simulations. *J. Phys. Chem. C* **2008**, *112*, 7631–7636.